Mon. Not. R. Astron. Soc. **000**, 000–000 (0000) Printed 2 February 2008 (MN LaTeX style file v2.2)

Dwarf galaxies in voids: Suppressing star formation with photo-heating

Matthias Hoeft[1], Gustavo Yepes[2], Stefan Gottlöber[3], and Volker Springel[4]
[1] *International University Bremen, Campus Ring 1, 28759 Bremen, Germany*
[2] *Grupo de Astrofisica, Universidad Autonoma de Madrid, Cantoblanco, 28039 Madrid, Spain*
[3] *Astrophysikalisches Institut Potsdam, An der Sternwarte 16, 14482 Potsdam, Germany*
[4] *Max-Planck-Institut für Astrophysik, Karl-Schwarzschild-Str. 1, Garching bei München, Germany*

arXiv:astro-ph/0501304v2 28 Jun 2006

ABSTRACT

We study structure formation in cosmological void regions using high-resolution hydrodynamical simulations. Despite being significantly underdense, voids are populated abundantly with small dark matter halos which should appear as dwarf galaxies if their star formation is not suppressed significantly. We here investigate to which extent the cosmological UV-background reduces the baryon content of dwarf galaxies, and thereby limits their cooling and star formation rates. Assuming a Haardt & Madau UV-background with reionisation at redshift $z = 6$, our samples of simulated galaxies show that halos with masses below a characteristic mass of $M_c(z = 0) = 6.5 \times 10^9\, h^{-1}\,\mathrm{M}_\odot$ are baryon-poor, but in general not completely empty, because baryons that are in the condensed cold phase or are already locked up in stars resist evaporation. In halos with mass $M \lesssim M_c$, we find that photo-heating suppresses further cooling of gas. The redshift and UV-background dependent characteristic mass $M_c(z)$ can be understood from the equilibrium temperature between heating and cooling at a characteristic overdensity of $\delta \simeq 1000$. If a halo is massive enough to compress gas to this density despite the presence of UV-background radiation, gas is free to 'enter' the condensed phase and cooling continues in the halo, otherwise it stalls. By analysing the mass accretion histories of dwarf galaxies in voids, we show that they can build up a significant amount of condensed mass at early times before the epoch of reionisation. Later on, the amount of mass in this phase remains roughly constant, but the masses of the dark matter halos continue to increase. Consequently, photo-heating leads to a reduced baryon fraction in void dwarf galaxies, endows them with a rather old stellar population, but still allows late star formation to some extent. We estimate the resulting stellar mass function for void galaxies. While the number of galaxies at the faint end is significantly reduced due to photo-heating, additional physical feedback processes may be required to explain the apparent paucity of dwarfs in observations of voids.

Key words: cosmology: theory – methods: numerical – galaxies: evolution – galaxies: formation

1 INTRODUCTION

Large regions of space that contain few or no galaxies can be clearly identified in modern spectroscopic redshift surveys. About 25 years ago, such 'voids' have been first discovered (Gregory & Thompson 1978; Joeveer et al. 1978; Kirshner et al. 1981), but it remains a challenge to explain why they are apparently so empty.

It is well known that hierarchical models of structure formation in standard cold dark matter (CDM) cosmologies produce large underdense regions in the distribution of matter (Peebles 1982; Hoffman & Shaham 1982; van de Weygaert & van Kampen 1993), but these underdense regions still contain structural elements and bound halos, even though the characteristic masses of these objects are several orders of magnitude smaller than corresponding ones found in average regions of the universe. Gottlöber et al. (2003) predicted that a typical $20\,h^{-1}\,\mathrm{Mpc}$ diameter void should contain up to 1000 halos with mass $\sim 10^9\ h^{-1}\,\mathrm{M}_\odot$ and still about 50 halos with mass $\sim 10^{10}\ h^{-1}\,\mathrm{M}_\odot$. Assuming a magnitude of $M_B = -16.5$ for the galaxy hosted by a halo of mass $3.6 \times 10^{10} h^{-1}\mathrm{M}_\odot$ (Mathis & White 2002) predict that about five such galax-

ies should be found in the inner regions of a typical void of diameter $20\,h^{-1}\,\mathrm{Mpc}$.

Over the last decade, there were many attempts to find dwarf galaxies in voids (Lindner et al. 1996; Popescu et al. 1997; Kuhn et al. 1997; Grogin & Geller 1999). An overall conclusion from these studies has been that faint galaxies do not tend to fill up the voids outlined by the bright galaxies. Peebles (2001) pointed out that the dwarf galaxies in the Optical Redshift Survey (ORS) follow the distribution of bright galaxies remarkably closely. Using the SDSS data release 2, Goldberg et al. (2005) measured the mass function of galaxies that reside in underdense regions. They selected galaxies as void members if they had less than three neighbours in a sphere with radius $7\,h^{-1}\,\mathrm{Mpc}$. More than one thousand galaxies passed their selection criterion (which differs slightly from the criterion used in the numerical simulations of Gottlöber et al. (2003) and in this paper). Their measurements are consistent with the predictions from the numerical simulations once the tendency of more massive halos to concentrate at the outer parts of voids (where they still may pass the nearest neighbour selection criterion) is taken into account. However, the observational situation is unclear for halo masses smaller than $\sim 10^{10} h^{-1} \mathrm{M}_{\odot}$. At present, there are no observational hints that a huge number of dwarf galaxies in voids may exist, despite the large number of small halos predicted by CDM models.

This finding resembles the 'substructure problem' in galactic halos (Klypin et al. 1999; Moore et al. 1999). A solution for both problems could arise from physical processes capable of suppressing star formation in dwarf galaxies. The two major effects proposed in this context are supernova feedback and heating of the gas in halos by the UV-background radiation. The latter increases the thermal pressure, and as a result, the gas in systems with $T_{\mathrm{vir}} \lesssim 10^4 - 10^5$ K can be evaporated out of halos (Umemura & Ikeuchi 1984; Dekel & Rees 1987; Efstathiou 1992; Babul & Rees 1992). Similarly, supernova feedback could drive a galactic outflow that removes a significant fraction of the gas in a dwarf galaxy (Dekel & Silk 1986; Couchman & Rees 1986). However, the efficiency of supernova driven winds depends strongly on the details of model assumptions (Navarro & Steinmetz 1997, 2000; Springel & Hernquist 2003). A general result is that low-mass systems are much more easily affected by supernova driven winds than larger ones (Mac Low & Ferrara 1999; Navarro & Steinmetz 2000).

During the epoch of reionisation, the gas temperature is raised to a few times 10^4 K. Rees (1986) argued that in dark matter halos with virial velocities around $\sim 30\,\mathrm{km\,s^{-1}}$ gas can then be confined in a stable fashion, neither able to escape nor able to settle to the centre by cooling. The gas in significantly smaller systems is thought to be virtually evaporated (Thoul & Weinberg 1996; Barkana & Loeb 1999). However, due to central self-shielding the evaporation of gas that has already cooled can be significantly delayed (Susa & Umemura 2004a,b). Using radiative transfer simulations, Susa & Umemura (2004b) pointed out that halos may contain a significant amount of stellar mass produced before reionisation occurred, even if their remaining gas mass is evaporated during reionisation.

In a 3D Eulerian adaptive mesh refinement simulation, Tassis et al. (2003) found that the global star formation rate was significantly reduced during the reionisation epoch. Their result also indicated that stellar feedback enhances this effect dramatically. Thus, an imprint of the epoch of reionisation may be expected for the stellar population in dwarf galaxies. Indeed, almost all dwarf galaxies appear to have an early epoch of star formation (Mateo 1998), but there is no distinct time at which star formation becomes generally suppressed (Grebel & Gallagher 2004).

In this paper, we use high-resolution hydrodynamical simulations of cosmological void regions to analyse the star formation and cooling processes of void galaxies. In particular, the simulations are well suited for studying the evolution of isolated dwarf galaxies from the epoch of reionisation to the present. This allows us to examine whether the UV background has a sufficiently strong effect on dwarf galaxies, keeping them faint enough such that their abundance can be reconciled with observations. We also determine the characteristic mass scale below which cooling is suppressed by the UV background. An analysis of the spatial distribution of dwarfs, the impact of supernova feedback, and the spectral properties of the stellar content of the formed dwarf galaxies will be discussed separately.

Our study is organised as follows. Details of our simulations are described in Section 2. In Section 3, we analyse first the baryon fraction as a function of both halo mass and redshift. Then we investigate the mass growth of the condensed phase which consists of both stars and cold dense baryons. We identify the characteristic mass below which halos are subject to evaporation. Finally, we estimate the galaxy mass function in void regions. We discuss and summarise our results in Section 4.

2 SIMULATIONS

2.1 Numerical method

Our simulations have been run with an updated version of the parallel Tree-SPH code GADGET (Springel et al. 2001). The code uses an entropy-conserving formulation of SPH (Springel & Hernquist 2002) which alleviates problems due to numerical over-cooling. The code also employs a new algorithm based on the Tree-PM method for the N-body calculations which speeds up the gravitational force computation significantly compared with a pure tree algorithm.

Radiative cooling processes for an optically thin primordial mix of helium and hydrogen are included, as well as photo-ionisation by an external, spatially uniform UV-background. The net change of thermal energy content is calculated by closely following the procedure of Katz et al. (1996) for solving the rate equations. We also use the set of cross sections cited in this paper, but adopt a slightly modified Haardt & Madau (1996) UV-background with heating rates as depicted in Fig. 1.

The physics of star formation is treated in the code by means of a sub-resolution model in which the gas of the interstellar medium (ISM) is described as a multiphase medium of hot and cold gas (Yepes et al. 1997; Springel & Hernquist 2003). Cold gas clouds are generated due to cooling and are the material out of which stars can be formed in regions that are sufficiently dense. Supernova feedback heats the hot phase of the ISM and evaporates cold clouds, thereby

Simulation name	Refinement levels	$M_{\rm gas}$ ($10^6\,h^{-1}\,{\rm M}_\odot$)	$M_{\rm dark}$ ($10^6\,h^{-1}\,{\rm M}_\odot$)	Particle number	Star fraction	Feedback parameters β	A	T_{SN}	$J_0^{\rm UV}$
void2	3	5.51	34.2	5,068,359	0.060	0.1	1000	10^8	0.95
basic	3	1.50	8.24	7,376,094	0.048	”	”	”	”
high-res	4	0.18	1.03	43,544,537	0.053	”	”	”	”
high-UV	3	1.50	8.24	7,390,626	0.024	”	”	”	95.0
low-UV	3	”	”	7,676,786	0.079	”	”	”	0.0095
no-UV	3	”	”	7,873,866	0.118	”	”	”	0.0
imp-heat-15	3	”	”	7,504,500	0.046	”	”	”	0.95
imp-heat-50	3	”	”	7,499,772	0.044	”	”	”	0.95
no-feedback	3	”	”	7,384,373	0.047	0	0	0	0.95

Table 1. Main characteristics of the void simulations. $M_{\rm gas}$ and $M_{\rm dark}$ denote the mass of a gas and of a dark matter particle in the simulation, respectively. Feedback parameters are according to model described in Springel & Hernquist (2003). The UV-flux, $J_0^{\rm UV}$, at $z = 0$ is given in units of $10^{-23}\,{\rm ergs\,s^{-1}\,cm^{-2}\,sr^{-1}\,Hz^{-1}}$. For the description of the simulation with an additional heat pulse see Sec. 3.2.

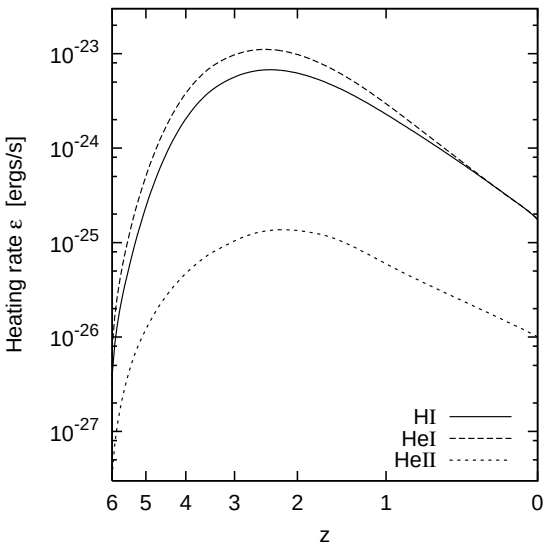

Figure 1. Photo-heating rates due to the ambient UV-background as a function of redshift. We adopt a time evolution for the UV-background as given by Haardt & Madau (1996). Reionisation in this model takes place at $z = 6$.

establishing a self-regulation cycle for star formation. The heat input due the supernovae also leads to a net pressurisation of the ISM, such that its effective equation of state becomes stiffer than isothermal, see Fig. 2. This stabilises the dense star forming gas in galaxies against further gravitational collapse, and allows converged numerical results for star formation even at moderate resolution. We also follow chemical enrichment associated with star formation, but we have neglected metal-line cooling in computing the cooling function. See Springel & Hernquist (2003) for a more detailed description of the star formation model implemented in the GADGET code.

2.2 Initial conditions

Using the mass refinement technique described by Klypin et al. (2001), we simulate void regions with high mass resolution, embedded in a proper cosmological environment. Our voids have been selected for resimulation from two periodic computational boxes of side-lengths $L = 80\,h^{-1}\,{\rm Mpc}$ and $50\,h^{-1}\,{\rm Mpc}$, respectively. To construct suitable initial conditions, we first created an unconstrained random realization at very high resolution, using the ΛCDM power spectrum of perturbations. For the large box, $N = 1024^3$ particles were used, while for the smaller box, we employed 2048^3 (~ 8.6 billion) particles. The initial displacements and velocities of the particles were calculated using all waves ranging from the fundamental mode $k = 2\pi/L$ to the Nyquist frequency $k_{\rm ny} = 2\pi/L \times N^{1/3}/2$. To produce initial conditions at lower resolution than this basic high-resolution particle set-up, we then merged particles, assigning to merged particles a velocity and a displacement equal to the average values of the original small-mass particles.

In this way, we first run 128^3 low-resolution simulations until the present epoch and selected the void regions from them. The algorithm for identifying the voids is described in detail in Gottlöber et al. (2003). It allows us to select void regions with arbitrary shape. To this end, the method starts from a spherical representation of the void which is then extended by spheres of smaller radius, which are added from the surface of the void into all possible directions. However, in the present application we have restricted the resimulation to a spherical void region to avoid ambiguities in the definition of allowed deviations from spherical shape.

In the second simulation step we use the original sample of small-mass particles in the regions of interest when we construct initial conditions. Thus we reach a mass resolution within the void regions that corresponds to the 1024^3 or 2048^3 set-up, respectively. We use a series of shells around the voids where we progressively merge more and more of the particles until the effective resolution of 128^3 particles is reached again far away from the voids. This procedure ensures that the voids evolve in the proper cosmological environment and with the right gravitational tidal fields. Mixing of particles of different mass occurs only in the shells surrounding the high resolution voids. Finally, we split the particles in the regions of high mass resolution into dark matter and gas particles. For all simulations, we adopted a concordance cosmological model with $\Omega_m = 0.3$, $\Omega_\Lambda = 0.7$, $\Omega_b = 0.04$, $h = H_0/(100\,{\rm km\,s^{-1}\,Mpc^{-1}}) = 0.7$ and $\sigma_8 = 0.9$.

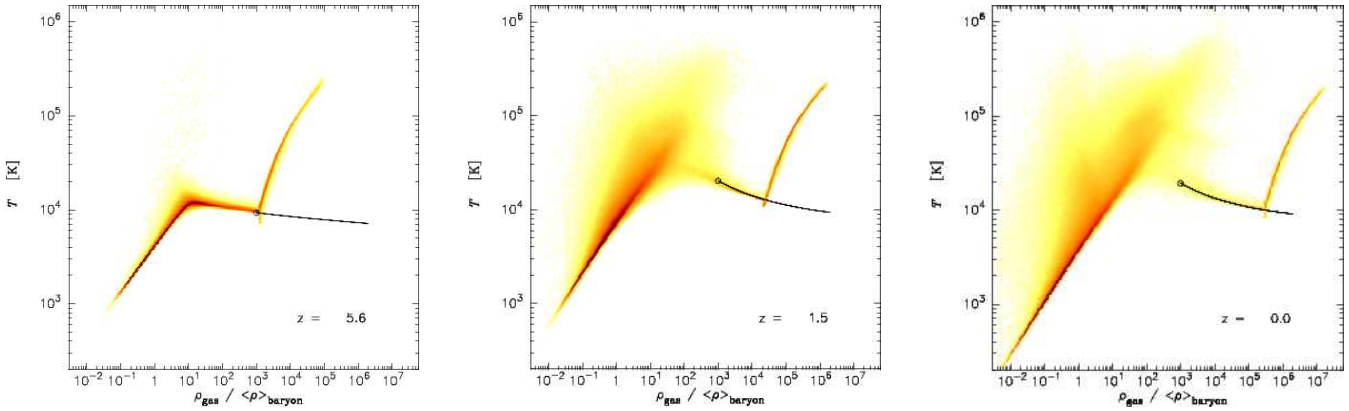

Figure 2. The distribution of particles in the density - temperature phase diagram for different redshifts for the high-res run. The solid curves give the equilibrium line. It is derived from the heating-cooling module in the code by computing the temperature at which the heating rate equals the net cooling rate. We assume that the 'entry' into the condensed branch occurs at $10^3\ \langle\rho_{\rm baryon}\rangle$. The circles indicate the derived entry temperatures for the individual redshifts. See Sec. 3.3 and Fig. 10 for a discussion of the equilibrium and entry temperatures.

2.3 Simulation runs

Using the multi-mass technique described above, we have re-simulated a void region in the $80\,h^{-1}$ Mpc box with three levels of refinement. The mass of a dark matter particle in the void is $3.4 \times 10^7\,h^{-1}\,{\rm M}_\odot$. The corresponding SPH gas particles have an initial mass of $5.5 \times 10^6 h^{-1}{\rm M}_\odot$. Note that some gas particles may reduce their mass during the run (or vanish entirely) if they undergo star formation and create new collisionless star particles. In our analysis of the simulation results, we in general only consider halos composed of a minimum of 150 dark matter particles. For the $80\,h^{-1}$ Mpc simulations this corresponds to a minimum halo mass of $5.1 \times 10^9\,h^{-1}\,{\rm M}_\odot$ and a circular velocity ~ 23 km/s.

We have also carried out re-simulations of a void region in the $50\,h^{-1}$ Mpc box. This leads to a substantially improved mass resolution with the same level of refinement. Here we achieve a mass resolution of $8.2 \times 10^6\,h^{-1}\,{\rm M}_\odot$ for the dark matter particles, corresponding to a minium halo mass of $1.2 \times 10^9\,h^{-1}\,{\rm M}_\odot$. In addition, we have evolved this region also with the full resolution available based on the initial high-resolution particle set-up (the 2048^3 particle grid, corresponding to four levels of refinement). In this case, the mass resolution is improved to $1.0 \times 10^6\,h^{-1}\,{\rm M}_\odot$ for the dark matter particles, and the minium halo mass reaches down to $1.6 \times 10^8\,h^{-1}\,{\rm M}_\odot$. We give an overview of our simulations in Table 1, where we also list the main simulation parameters.

Power et al. (2003) gave a simple criterion for the gravitational softening length necessary in N-body simulations, $\epsilon \gtrsim r_{200}/\sqrt{N_{200}}$. Obeying this condition ensures that particles do not suffer stochastic scattering in the periphery of the halo which exceed the mean gravitational acceleration. Power et al. (2003) found that even a larger softening length keeps the central density profile unaffected. However, in a hydrodynamical simulation including radiative cooling we wish to use a softening as small as possible to obtain an optimal resolution for the cooled gas. Our halos are in the mass range from about $10^9\,h^{-1}\,{\rm M}_\odot$ to $10^{11}\,h^{-1}\,{\rm M}_\odot$. Using

$$M_{200} = 200 \times \frac{4}{3}\pi r_{200}^3\,\langle\rho\rangle,$$

where $\langle\rho\rangle$ is the average cosmic matter density, we find the corresponding softening lengths, $\epsilon \sim 2.2$ to $1\,h^{-1}$ kpc. Since we carry out simulations including radiative cooling we lower the softening slightly and use for all simulations the maximum between $2\,h^{-1}$ kpc comoving and $0.8\,h^{-1}$ kpc physical. For the very high-resolution run, the parameters $1\,h^{-1}$ kpc and $0.5\,h^{-1}$ kpc, respectively, are used. We have imposed a minimum SPH smoothing length equal to the gravitational softening length.

In order to analyse in more detail the effects of the UV-background on the baryonic content of halos, we have also carried out several additional runs of our basic simulation of the void identified in the $50\,h^{-1}$ Mpc box. Here we used different choices for the star formation and feedback parameters, and three different values of the UV-flux normalisation, spanning four orders of magnitude. We also ran the same simulation without thermal stellar feedback. Using this run we can demonstrate that thermal feedback itself has only a minor impact on the halo baryon fraction. For all simulations with star formation and feedback, we selected similar parameters for the multiphase model of the ISM as used by Springel & Hernquist (2003). However, we here have not included kinetic feedback (wind model) from supernova, since then it would be difficult to disentangle the effects caused by the UV background from those caused by supernova driven winds.

The simulations were performed on parallel supercomputers, an IBM Regatta p690 (Jülich Supercomputer Center, Germany), a SGI Altix 3700 (CIEMAT, Spain) and on several different Beowulf PC clusters at the AIP and IU Bremen. The typical CPU time for a simulation with up to 5 million particles was $\sim$ 9 CPU days on an SGI ALTIX with 32 processors. The highest resolution simulation with 44 million particles was run on an AMD Opteron Beowulf cluster and took a little less than 2 months of CPU time using 64 processors.

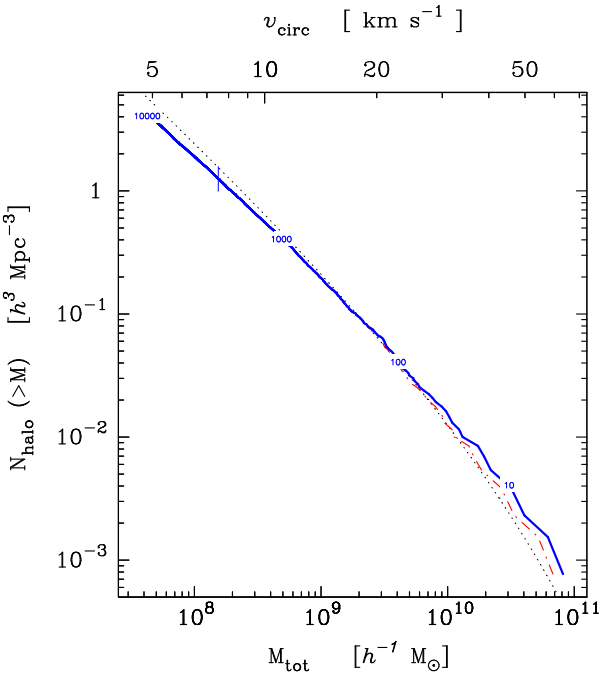

Figure 3. Mass function $n(> M)$ for our basic run halo sample at $z = 0$. The mass function is derived by taking into account the total mass within the virial radius. The small vertical line indicates a mass of 150 dark matter particles, which we consider as a lower limit for an acceptable resolution. The numbers along the line indicate the actual number of halos. The dashed line is obtained by considering the dark matter mass instead of the total mass. For comparison the modified Sheth-Tormen mass function derived by Gottlöber et al. (2003) is shown (dotted line). For our halo sample, the circular velocity $v_{\rm circ} = GM_{\rm tot}/r_{\rm vir}$ can be well approximated by $v_{\rm circ} = 31\,{\rm km\,s^{-1}} \times (M_{\rm tot}/10^{10}\,h^{-1}\,M_\odot)^{0.34}$.

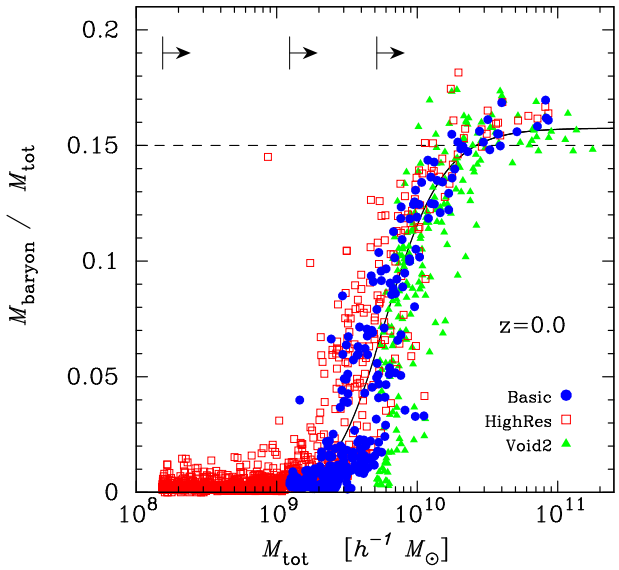

Figure 4. Baryon fraction in individual halos for differently resolved simulations. We compute for each halo the baryon fraction within the virial radius, $(M_* + M_{\rm gas})/(M_* + M_{\rm gas} + M_{\rm dm})$. We take only those halos into account which consist of more than 150 dark matter particles. From the left to the right the arrows indicate the smallest resolved halos in the high-res, basic, and void2 run, respectively. For the high-res run we approximate the baryon fraction by Eq. (5) (solid line).

3 SIMULATED DWARF GALAXIES IN VOIDS

3.1 Halo mass function

We identify virialised halos using the Bound Density Maxima (BDM) algorithm (Klypin et al. 1999). In this method, galaxy halos are found from local density maxima with an iterative procedure to identify the centre of mass in a small sphere around the centre. Then, radial density profiles are computed. Particles that are not gravitationally bound to the system are excluded in the computation of the total mass. The radius of the system is selected as the minimum between the virial radius and the point at which the density profile stops declining (e.g. because a nearby halo is encountered, or the halo lies within another halo). We define the virial radius as the radius where the enclosed mean density equals the value expected for a top-hat collapse model,

$$\frac{M_{\rm vir}}{4/3\,\pi\,r_{\rm vir}^3} = \Delta_c(z)\,\langle\rho\rangle, \qquad (1)$$

where $\langle\rho\rangle$ is the mean cosmic matter density. For the case of a flat cosmology with $\Omega_m + \Omega_\Lambda = 1$, a useful approximation for the redshift dependent characteristic virial overdensity is given by Bryan & Norman (1998):

$$\Delta_c(z) = \frac{178 + 82\,x(z) - 39\,x^2(z)}{1 + x(z)}, \qquad (2)$$

$$x(z) = -\frac{(1-\Omega_m)\,a^3}{\Omega_m + (1-\Omega_m)\,a^3}, \qquad (3)$$

with the cosmological expansion factor $a = 1/(z+1)$. The mean density $\langle\rho\rangle$ evolves with redshift as

$$\langle\rho\rangle(z) = \Omega_m\,\rho_{\rm crit,0}\,\frac{1}{a^3} = \Omega_m\,\frac{1}{a^3}\,\frac{3H_0^2}{8\pi G}. \qquad (4)$$

In low density regions, the number of interacting halos or halos with substructure is very small. Thus, the radii of virtually all our objects correspond to their spherical-overdensity virial radii. For the same reason, the fraction of unbound particles in the halos is small. Hence, we can simply consider all particles within the virial radius to compute further halo properties.

In Figure 3, we show the cumulative mass function for our sample of void halos, based on the measured total virial masses. For comparison, we also include a line for the dark matter halo mass function alone, which however shows appreciable differences only for the most massive halos. Gottlöber et al. (2003) derived a modified Sheth-Tormen mass function for halo populations in underdense regions. They showed that the mass function can be derived from the mean density, $\Omega_{m,\rm void}$, in the volume considered. For our halo sample analysed here (based on the high-res run), the relevant mean density amounts to $\Omega_{m,\rm void} \simeq 0.03$. The predicted mass function for this value is in good agreement with the one measured for the simulated halo sample. Our simulations thus are in good agreement with conclusion obtained in previous works: Voids are filled with a significant number of halos with masses $M \lesssim 10^{10}\,h^{-1}\,{\rm M}_\odot$. If each of these halos contains the mean cosmic baryon fraction, and

cooling and star formation within them is not suppressed significantly, a high density of luminous dwarf galaxies should be expected in voids.

3.2 Baryon content of dwarf galaxies

In Figure 4, we show the baryonic mass fraction, $f_b = M_{\rm baryon}(< r_{\rm vir})/M_{\rm tot}(< r_{\rm vir})$, for each halo identified in our simulated voids. The more massive halos in our sample, $M_{\rm tot} \gtrsim 2 \times 10^{10}\ h^{-1}\ {\rm M}_\odot$, have approximately the cosmic mean baryon fraction, $f_{b,{\rm cosm}} = \Omega_b/\Omega_m$. However, for smaller halos, the baryon fraction decreases rapidly with decreasing halo mass. In fact, most of the smallest halos are nearly free of baryons.

We find that the baryon fraction is insensitive to the details of the definition of the virial radius of halos, because the cumulative baryon fraction varies only very slowly in the outskirts of halos. This can be seen in Figure 5, where we show the radial profile of the baryon fraction for halos of different mass. While the sizes of halos can be systematically affected by different definitions of the virial radius (one may for example choose to use only the dark matter for the definition and not the total mass), the measured baryonic fractions are robust.

We quantify the transition between the two extremes, 'baryon-rich' and 'baryon-poor', using the fitting function proposed by Gnedin (2000),

$$f_{\rm b} = f_{b0}\ \left\{1 + (2^{\alpha/3} - 1)\ \left(\frac{M_c}{M_{\rm tot}}\right)^{\alpha}\right\}^{-3/\alpha}, \qquad (5)$$

where f_{b0} is the asymptotic baryon fraction in massive halos. Figure 6 indicates that a baryon fraction decreasing with mass can be reasonably well approximated assuming $\alpha = 2$ in Eq. (5). Gnedin (2000) found a less steep transition, which may be caused by radiative transfer effects included in his code. A partial self-shielding in halos may then reduce the radiative heating. For very small halos the approximation seems to fail in any case. We discuss a possible origin for this in Sec. 3.5.

In the very massive halos of our samples we found a roughly constant baryon fraction f_{b0}, independent of redshift and numerical resolution. The value of $f_{b0} \sim 0.16$ we measured lies slightly above the cosmic mean. At the characteristic mass, M_c, the baryon fraction is $f_{\rm b} = f_{b0}/2$ by definition. For $z = 0$, we derive a characteristic mass of $M_{\rm c} = 6.5 \times 10^9\ h^{-1}\ {\rm M}_\odot$ from the 'high-res' run.

It is important to consider whether numerical resolution effects influence this result. In particular, a too small number of resolution elements per halo could easily introduce a spurious baryon reduction due to numerical oversmoothing. The resulting characteristic mass would then depend on the number of particles in a halo rather than on the halo mass itself when simulations with quite different mass resolutions are compared. In Fig. 4, we compare the void2, basic and high-res runs. Their baryon fractions as a function of halo mass overlap nicely, even though the mass resolution differs by more than an order of magnitude. Therefore, significant numerical oversmoothing occurs only in halos smaller than those included in our analysis.

The marginal displacement of the characteristic mass as a function of resolution can be understood in terms of the better resolved merging histories of higher resolution runs. The better the mass resolution, the more small progenitors of a final halo can be resolved and contribute stars to the final object. In particular, many more star particles are formed while the UV-background radiation is still vanishingly small. The resulting difference can be seen in Tab. 1: The basic and the high-res run have identical initial conditions, except for the increased resolution, which leads to the production of $\sim 10\%$ more stars. As a result, the characteristic mass of the high-res run is also slightly lowered. However, this effect is limited by the fraction of mass in progenitors which can form stars before reionisation.

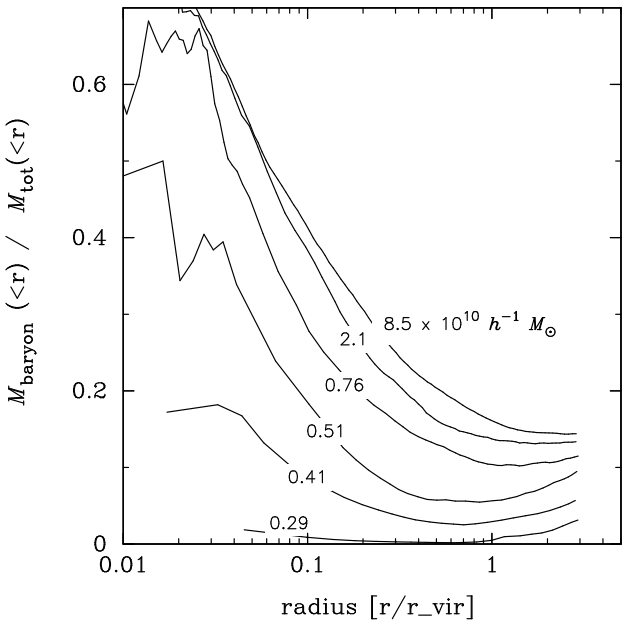

Figure 5. The baryon fraction as a function of radius for halos with different mass. All halos are chosen at $z = 0$ from the basic simulation. Radii are normalised to the BDM virial radius. Labels along the lines indicate the mass of the halos.

The importance of the UV-background for the baryon fraction is demonstrated in Fig. 7. We have carried out three simulations for which we multiplied our standard UV-flux for every redshift by the factors 0.0, 0.01, and 100, keeping the spectral shape of the UV-background radiation constant. These strong variations of the UV-background flux level displace the characteristic mass-scale only by a factor $\lesssim 3$. We will discuss in the next section, Sec 3.3, that this shift is caused by the modification of the equilibrium temperature. The run with zero UV-flux clearly shows that the background radiation causes the baryon deficit: In this case, even the smallest halos show the average cosmic baryon fraction.

During the epoch of reionisation, the true heat input may be larger than computed in our heating-cooling scheme, which is based on the assumption of collisional ionisation equilibrium. In the onset of reionisation, non-equilibrium effects can be significant, however, and the ionised fraction increases very rapidly. While our implicit solver for the evolution of the thermal energy deals gracefully with this situation, part of the injected energy may be missed if the ionized fraction jumps from zero to a finite value in the course of one time step. One may speculate that the heat pulse at

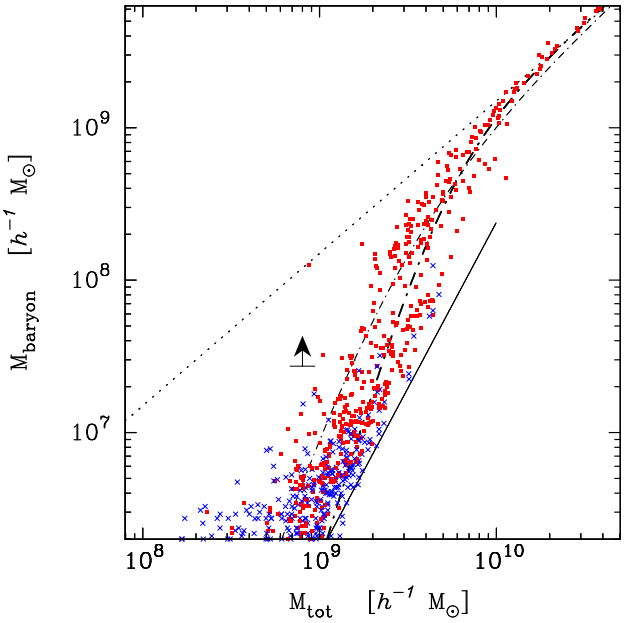

Figure 6. The baryon mass as a function of the total mass enclosed in the virial radius from the high-res run. Solid squares indicate halos with stars, and crosses those without. The dotted line shows the dependence if each halo would contain the mean cosmic baryon fraction. The solid line is derived based on the assumption that in low-mass halos the gas density follows the average distribution in the ρ-T diagram (see Sec. 3.5 for more details). The arrow indicates a baryon mass consisting of 150 SPH particles. The properties of smaller halos may be affected by the poor SPH resolution in these halos. Thin and thick dash-dotted lines show the approximation of Eq. (5), with exponents $\alpha = 1$ and 2, respectively.

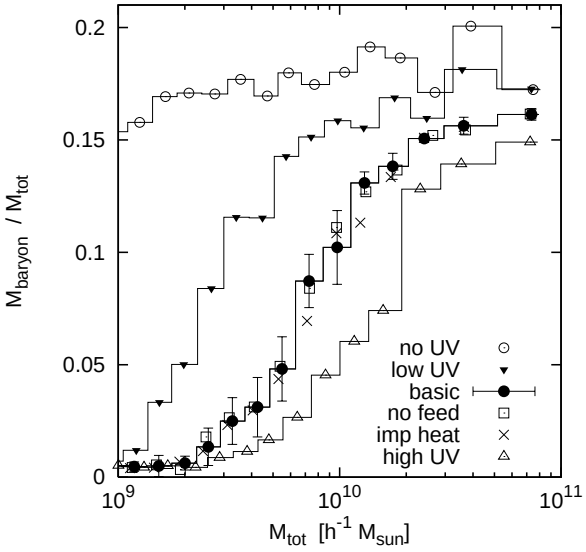

Figure 7. Baryon fraction as a function of mass for different UV-fluxes. The photo-heating by the UV-background is varied from zero to $J_0^{\rm UV} = 95 \times 10^{-23}$ ergs s^{-1} cm^{-2} sr^{-1} Hz^{-1}, see Tab. 1. The average baryon fraction in mass bins is computed; for the basic-run also the r.m.s. deviation is shown by error bars. In addition baryon fractions are depicted for the impulsive heat model with 1.5×10^4 K (imp heat) and for the simulation without thermal stellar feedback (no-feed).

reionisation is underestimated by our method, but that it may have a significant effect on the baryon fraction in the halos later on if fully taken into account. In order to test this question, we have carried out two simulations which mimic an upper limit for the impulsive heat input: from $z = 7$ to 6, all gas is heated to a minium temperature of 1.5×10^4 K and to 5.0×10^4 K in the runs imp-heat-15 and imp-heat-50, respectively. After z=6 the gas evolves again according to our standard heating-cooling scheme, see Fig. 8. Even with a strong heat input at the epoch of reionisation, our measured characteristic mass at $z = 0$ is hardly affected, as can be seen in Fig. 7. Moreover, the different heat input at reionisation has virtually no effect on the evolution of the characteristic mass. This is caused by the short cooling times at high redshift: Fully ionised gas with average cosmic density and a temperature of 5.0×10^4 K has at $z = 6$ a cooling time as short as ~ 50 Myr, because the maximum of hydrogen line cooling is in this temperature range. Inverse Compton cooling with CMB photons is also very efficient at these redshifts. It keeps the cooling times short even if we would heat to a temperature above the efficient line cooling. Since gas in the halo of a galaxy is much denser, the cooling time is even shorter. Hence, the energy injected by a heat-pulse at the epoch of reionisation is radiated away on time-scales smaller than the dynamical ones.

Finally, efficient stellar feedback can in principle also remove gas from small halos. However, for the thermal feedback considered in the multiphase feedback model used in our simulations, such a gas removal does not occur. While the feedback regulates the consumption of cold gas by star formation, it does not cause gaseous outflows. The latter only occur in our simulations if explicitly modeled with a kinetic feedback component (Springel & Hernquist 2003). However, we deliberately avoided the inclusion of such feedback models in this study, allowing us to focus on the impact of UV-heating in a clean fashion. Figure 7 verifies that in simulations without feedback the characteristic mass scale is at the same place as in the basic run.

In order to determine the evolution of characteristic mass with redshift, we use a least-square fit of Eq. (5) to our measurements of the baryon mass fraction at a number of different simulation output times. We can infer the transition mass scale reasonably well from our high-res simulation up to $z \sim 5$. In Fig. 9, we show the resulting evolution of $M_c(z)$. Interestingly, as structure grows towards lower redshifts, progressively more massive halos become baryon-poor.

It is interesting to also compare this result with the time evolution of M_c measured for the simulation with an additional heat pulse at the epoch of reionisation, which is also shown in Figure 9. The two curves are identical except for a small offset. As discussed above, the latter can be attributed to the different mass resolutions of the two simulations. The similarity of the two curves therefore shows that the heat pulse at reionisation does at most weakly influence the characteristic mass at $z \lesssim 3$. $M_c(z)$ is relatively insensitive at these redshifts to the previous thermal history of the low density gas at high redshift, but it depends more strongly on the current state of the gas and that of the UV background.

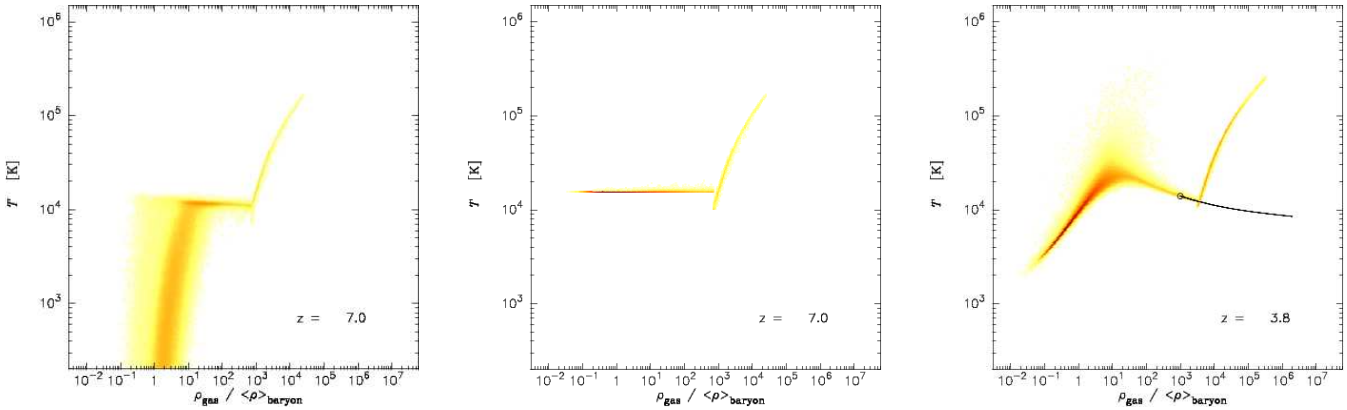

Figure 8. The distribution of particles in the density - temperature phase diagram for different redshifts for the impulse-heat-15 simulation. From $z = 7$ to 6 the minimum gas temperature is set to 1.5×10^4 K. For smaller redshift the standard heating-cooling scheme is applied. At $z \sim 4$ the initial heat pulse is faded away by adiabatic cooling for densities $\rho_{\rm gas}/\langle\rho\rangle_{\rm baryon} \gtrsim 0.1$. Equilibrium and entry temperatures are indicated by the solid lines and open circles, respectively. See Sec. 3.3 and Fig. 10 for a discussion of them.

The evolution of the characteristic mass $M_{\rm c}(z)$ can be expressed as

$$\frac{M_{\rm c}(z)}{10^{10}\,h^{-1}\,M_\odot} = \left\{\tau(z)\,\frac{1}{1+z}\right\}^{3/2}\,\left\{\frac{\Delta_c(0)}{\Delta_c(z)}\right\}^{1/2}, \qquad (6)$$

were $\tau(z)$ encodes the evolution of the minimum virial temperature required for halos to still allow further cooling in the presence of the UV-background. We will discuss this criterion and its derivation in more detail below. Treating $\tau(z)$ as a simple analytic fitting function for the moment, we find that our numerical results can be well described by

$$\tau(z) = 0.73 \times (z+1)^{0.18}\,\exp\{-(0.25\,z)^{2.1}\} \qquad (7)$$

for the 'high-res' run over the entire redshift range, see Fig. 9.

3.3 How to suppress gas condensation

A quantitative understanding of the characteristic mass can be obtained by considering the equilibrium line between photo-heating rate and cooling rate in the density-temperature phase-space plane. In Figure 2, we show the gas particles at three different times, and include this equilibrium line for high-density gas, computed self-consistently from the cooling and heating routines in GADGET. Much of the gas in the density range $\delta \sim 10^3 - 10^6$ is indeed distributed along this line.

We define the equilibrium temperature at a fiducial overdensity of 1000 as "entry temperature" $T_{\rm entry}$ into the condensed phase. Gas that condenses in a halo will at least reach this temperature due to photo-heating before it can cool further to the $\simeq 10^4$ K reached at very high overdensities. Note that this is independent of the potential difference between a "cold mode" or a "hot mode" of accretion (Kereš et al. 2005). In the cold mode, gas creeps along the lowest possible temperature into the condensed phase, without being heated by an accretion shock to the virial temperature first, as it happens in the "hot mode". However, even in the cold mode, the gas will at least be heated to the "entry temperature" $T_{\rm entry}$ by the UV-background. After reaching this temperature, it can then evolve along the equilibrium line towards higher densities and eventually reach the onset of star formation. In a sense, for halos with $T_{\rm vir} = T_{\rm entry}$, the hot and cold mode should therefore become largely identical.

We argue that a comparison of $T_{\rm vir}$ with $T_{\rm entry}$ provides a simple criterion that tells us whether the gas in a halo can still cool. To demonstrate this, we show that this assumption provides a quantitative explanation for our measurements of $M_c(z)$. We define the virial temperature for our halos as

$$k_{\rm B}T_{\rm vir} = \frac{1}{2}\mu m_{\rm p}\frac{GM_{\rm vir}}{r_{\rm vir}}, \qquad (8)$$

where $m_{\rm p}$ is the proton mass and $k_{\rm B}$ is the Boltzmann constant. The mean molecular weight of the fully ionised gas is $\mu = 0.59$. Virial mass and radius are related by the definitions of Eqs.(1) and (4). Hence the virial temperature depends on the mass as

$$T_{\rm vir} = \frac{1}{2}\frac{\mu m_p}{k_B}\left\{\frac{\Delta_c(z)\Omega_m}{2}\right\}^{\frac{1}{3}}(1+z)\,\{GM_{\rm vir}H_0\}^{\frac{2}{3}}. \qquad (9)$$

For the cosmological concordance model used here we insert $\Omega_m = 0.3$ and cast Eq. (9) into

$$T_{\rm vir} = 3.5 \times 10^4\ {\rm K}\ (1+z)\left\{\frac{\Delta_c(z)}{\Delta_c(0)}\right\}^{\frac{1}{3}}\left\{\frac{M_{\rm vir}}{10^{10}h^{-1}M_\odot}\right\}^{\frac{2}{3}}. \qquad (10)$$

Now we apply our criterion introduced above: If the virial temperature of a halo is below the entry temperature into the condensed phase, its potential well is not deep enough to compress the gas sufficiently and to overcome the pressure barrier generated by the photo-heating. Thus, we expect that the characteristic halo mass necessary to increase the condensed baryonic mass can be estimated by rewriting Eq. (10) into

$$\frac{M_{\rm c}(z)}{10^{10}\,h^{-1}M_\odot} \simeq \left\{\frac{T_{\rm entry}(z)}{3.5\times10^4\ {\rm K}}\frac{1}{1+z}\right\}^{\frac{3}{2}}\left\{\frac{\Delta_c(0)}{\Delta_c(z)}\right\}^{\frac{1}{2}}. \qquad (11)$$

This relation can only be an approximation, since $M_c(z)$ will in general depend on the entire history of a halo, whereas $T_{\rm entry}$ is an instantaneous quantity. However, we have seen from the 'imp-heat' simulation that the characteristic mass is mainly determined by the current state of the gas. We

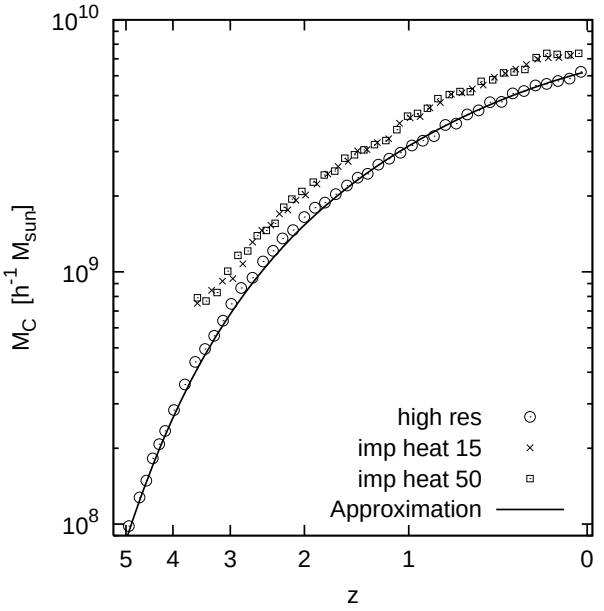

Figure 9. Evolution of the characteristic mass scale M_c for several simulations. We approximate the halo baryon fractions for each simulation by Eq. (5). We determine M_c using a least-squares method. f_{b0} is a free parameter, but it is almost constant for all simulations, $f_{b0} \sim 0.16$. Open circles indicate the results for the high-res simulations. Here the smallest halos included have $1.5 \times 10^8\, h^{-1}\, M_\odot$. Crosses and squares show the results for imp-heat-15 and imp-heat-50 simulations, respectively. Here the smallest halos included have $10^9\, h^{-1}\, M_\odot$. Note that the characteristic mass may lie somewhat below the mass of the smallest halos, since it is derived from a fit to the baryon fractions. The solid line shows the approximation for $M_c(z)$ from the high-res run using Eq. (6) and (7).

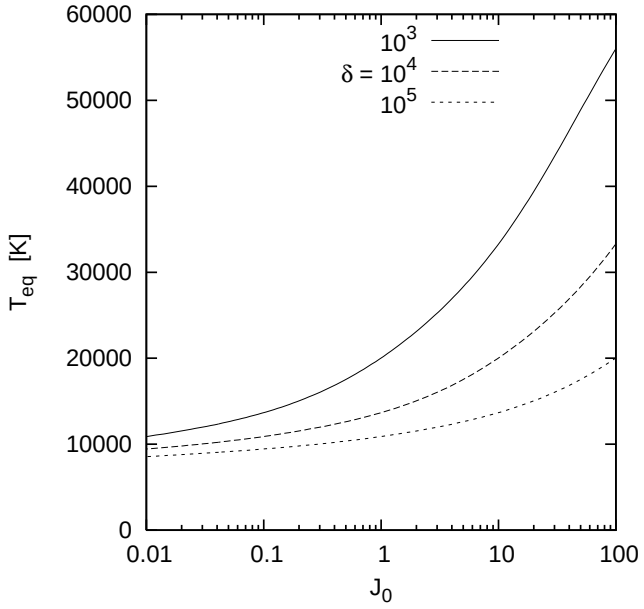

Figure 10. The equilibrium temperature, $T_{\rm eq}$, as a function of the amplitude, J_0, of the UV-background radiation. $T_{\rm eq}$ is computed by solving $\mathcal{H}(T_{\rm eq}, \rho) = \Gamma(T_{\rm eq}, \rho)$. Heating and cooling functions as implemented for the numerical simulations are used. The amplitude dependence is given for three densities, $\rho = \delta \Omega_{\rm b} \rho_{\rm crit}$, for $z = 0$.

therefore assume that $M_c(z)$ can be considered as an instantaneous quantity. In this sense, Eq. (11) gives the motivation for our ansatz of Eq.(6). Also it shows that in a first approximation the fitting function $\tau(z)$ is proportional to $T_{\rm entry}(z)$.

In Figures 2 and 8 solid lines indicate the equilibrium temperature, $\mathcal{H}(T_{\rm eq}, \rho) = \Gamma(T_{\rm eq}, \rho)$, for $\delta > 10^3$. In that density region cooling times are short and the gas is essentially distributed along the equilibrium line –or according to the multi-phase ISM prescription used in GADGET-2. The equilibrium temperature depends on the UV-background. The dependency on the amplitude of the background radiation, J_0, is shown in Fig. 10. If we lower or increase the UV-flux by two orders of magnitude, the entry temperature shifts roughly by a factor of two. With $M_c \propto T_{\rm entry}^{3/2}$ we obtain the shift of M_c as found in the simulations, see Sec. 3.2 and Fig. 7.

In the following, we use the abbreviation $\tilde{T}_{\rm entry} = T_{\rm entry}(z)/3.5 \times 10^4$ K. In Figure 11, we show the evolution of $\tilde{T}_{\rm entry}(z)$ for the high-res run and compare it with the expression for $\tau(z)$ derived from fitting the measured redshift evolution of the characteristic mass in the same simulation. First of all, we note that the redshift variation of both is small compared with the evolution of the characteristic mass. This indicates that the large variation of the latter is mainly governed by the $1/(z+1)$ term in Eq. (6). Furthermore, from Fig. 11 we can conclude that the simple criterion invoked above reproduces the evolution of $M_c(z)$ up to $z \sim 5$ astonishingly well, with a deviation of a few 10 %.

However, the condition $T_{\rm vir} = T_{\rm entry}$ appears to underestimate the characteristic mass for small redshift to some extent. This is not surprising for a number of reasons. For example, we compute the virial radius from the dark matter distribution only, hence the total masses used here are slightly above the virial masses. Furthermore, $T_{\rm entry}(z)$ determined at a fixed overdensity 1000 may underestimate the true entry temperature. We can account for this and improve our match of the numerical results by refining our criterion in the following way: The virial temperature of a halo has to be $\gtrsim 1.3 \times T_{\rm entry}$ to permit further condensation.

To explain the deviation at high redshifts we have to acknowledge the fact discussed above: $\tau(z)$ and $\tilde{T}_{\rm entry}$ are completely different in the sense that the latter denotes which halos are able to add more gas to the condensed phase at a given time, while the former reflects the entire evolution history of dwarf halos. Before reionisation, no halo is photo-evaporated, i.e. $M_c = \tau = 0$. It takes some time after reionisation to produce baryon-poor halos. Hence, $\tau(z)$ should be below $T_{\rm entry}$ for some time after reionisation.

In any case, the agreement demonstrated in Figure 11 shows that the argument that the virial temperature should at least equal the entry temperature provides a good quantitative description for the transition scale between baryon-poor and baryon-rich halos. Interestingly, this explanation can account for the effect simply by alluding to the ongoing photo-heating of the gas by the UV-background radiation, and the accompanying increase of the gas pressure in low mass halos. At $z \lesssim 3$ the effects of the impulsive heating

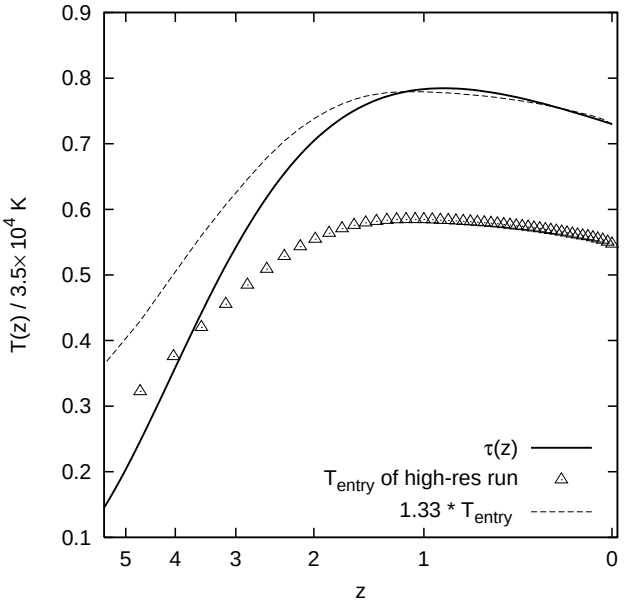

Figure 11. Evolution of the entry temperature. We derive from the high-res run the entry temperature, $T_{\rm entry}$, for several redshifts (open triangles). $T_{\rm entry}$ is determined according to the description in the caption of Fig. 2. For comparison we plot the expression $\tau(z)$ given in Eq. (7) (solid line). The scaled entry temperature ("refined model") is also shown (dashed line).

during the epoch of reionisation play only a subdominant role.

3.4 Baryon deficit in the linear theory

Small-scale baryonic fluctuations grow slower than the corresponding dark matter fluctuations due to the counteracting pressure gradients. To describe this effect, Gnedin & Hui (1998) introduced a filtering wavenumber $k_{\rm F}$ over which baryonic fluctuations are smoothed out. Gnedin (2000) compared the corresponding filtering mass

$$M_{\rm F} = \frac{4\pi}{3}\langle\rho\rangle\left(\frac{2\pi a}{k_{\rm F}}\right)^3 \qquad (12)$$

up to $z = 4$ with the characteristic mass measured in cosmological reionisation simulations and found a good agreement.

Gnedin & Hui (1998) showed that $k_{\rm F}$ can be related to the linear growth function $D(t)$ by

$$\frac{1}{k_{\rm F}^2} = \frac{1}{D}\int_0^t dt'\,\frac{c_{\rm s}^2(\ddot{D}+2H\dot{D})}{4\pi G\langle\rho\rangle}\int_{t'}^t dt''\,\frac{1}{a^2}, \qquad (13)$$

with the time-dependent Hubble parameter $H = \dot{a}/a$. We rewrite Eq. (13) in order to integrate it up to $z = 0$. The linear growth function obeys the relation

$$\ddot{D} + 2H\dot{D} = 4\pi G\langle\rho\rangle\, D, \qquad (14)$$

which we can use to remove the time derivatives in Eq. (13). We also substitute the integration variable by a. With

$$\left(\frac{H(a)}{H_0}\right)^2 = S^2(a) = 1 + \Omega_m\left(\frac{1}{a}-1\right) + \Omega_\Lambda(a^2+1) \qquad (15)$$

we then get

$$\frac{1}{k_{\rm F}^2} = \frac{1}{D}\int_0^a da'\,\frac{c_{\rm s}^2}{H_0^2}\,\frac{D}{S}\int_{a'}^a da''\frac{1}{a''^2 S} \qquad (16)$$

For a given cosmology the linear growth function can be computed by (Carroll et al. 1992)

$$D(a) = \frac{5}{2}\Omega_m\,\frac{S(a)}{a}\int_0^a da'\,\frac{1}{S^3(a)}, \qquad (17)$$

hence we obtain a solution for Eq. (13) for any redshift, provided the evolution of the sound speed, $c_{\rm s}(a)$, is known. To obtain the sound speed for the high-resolution region in the simulations we follow again Gnedin & Hui (1998) and compute the volume averaged temperature,

$$c_{\rm s}(a) = \frac{5}{3}\frac{k_{\rm B}\langle T\rangle_{\rm vol}(a)}{\mu m_{\rm p}}. \qquad (18)$$

Figure 12 shows that $\langle T\rangle_{\rm vol}$ rises sharply at the time of reionisation, thereafter it decreases slowly from $\sim$ 5000 K to 1000 K. These temperatures are lower than expected for an average cosmic volume because the considered void region is underdense and the temperature scales with density (see Fig. 2).

In Fig. 12, we show the resulting filtering mass scale. For redshift $z = 0$, it is about three times larger than the characteristic mass obtained from the simulations, while the difference becomes progressively smaller towards higher redshift. One may argue that the underdensity of the void region has to be taken into account. To consider a rather extreme case we assume that the void evolves like an open universe with $\Omega_m = 0.03$ and unchanged $\Omega_\Lambda = 0.7$. As shown in Fig. 12 (dashed line) the density of the region has only a moderate effect on the filtering mass. It reduces to some extent the difference with our measured characteristic masses. At a first glance one may expect a different density dependence of $M_{\rm F}$. The average density enters Eq. (12) directly via its appearance in the denominator of Eq. (13). If the density did not affect the Hubble constant, H, and the linear growth function, D, we would expect the filtering mass is proportional to $\langle\rho\rangle^{-1/2}$. However, H and D depend on $\langle\rho\rangle$ as can be seen from Eq. (14). In order to derive consistently the filtering mass as a function of Ω_m the density dependence of H and D, as given in Eqs. (15) and (17), has to be taken into account. For high redshift, $a \ll 1$, we can approximate

$$S^2(a) \sim \Omega_m\frac{1}{a}.$$

This leads to

$$\frac{1}{k_{\rm F}^2} \propto \frac{1}{\Omega_m}$$

and hence

$$M_{\rm F} \propto \Omega_m^{-1/2}.$$

For high redshift we obtain the same proportionality as expected without taking the contribution of H and D into account. However, the result changes for lower redshifts. For $a = 1$ we have $S = 1$, i.e. there is no dependence on Ω_m. This implies that the integral Eq. (16) depends less strong on Ω_m and in $M_{\rm F}$ the factor $\langle\rho\rangle$ becomes dominant.

In summary, we expect that at high redshift the filtering mass shows the proportionality $M_{\rm F} \propto \Omega_m^{-1/2}$, whereas for low redshift even the opposite behavior may occur. The

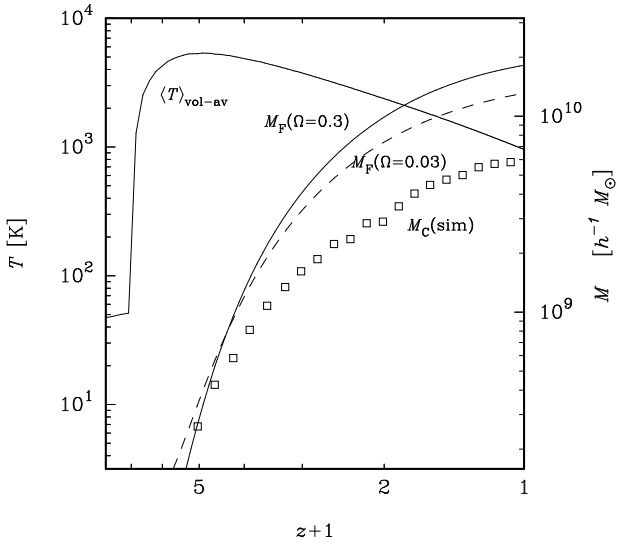

Figure 12. Comparison of filtering and characteristic mass. The thin line indicates the evolution of the volume averaged temperature in the simulation. The thick solid line gives the filtering mass integrated according to Eq. (16) using the averaged temperature depicted here. The dashed line shows the filtering mass for a low density region with $\Omega_m = 0.03$. Open squares indicate the characteristic mass obtained from the high-res simulation.

actual dependence can only be found by computing the integral in Eq. (13). Note that the speed of sound c_s is also a function of redshift and modifies the integral additionally. The dashed line in Fig. 12 gives the result for a low density region with $\Omega_m = 0.03$ and for the rather low average temperature in the void region. At low redshift the filtering mass overpredicts significantly the characteristic mass we measure.

The density dependence in Eq. (12) is partially compensated by the fact that for $a \ll 1$ the filtering wave number scales with density according to $k_{\rm F}^2 \propto \Omega_m$. In conclusion, we find that at low redshift the filtering mass $M_{\rm F}$ overpredicts the characteristic masses we measure.

3.5 Are there dark halos free of baryons?

We argued above that photo-heating may prevent further gas condensation in dwarf halos. If it never takes place in a given halo, or an existing condensed phase has been evaporated at some time by the UV-background, the halo will only contain diffuse gas, where "diffuse" for our purposes denotes gas of too low density to support star formation. It is therefore also interesting to distinguish between halos with and without stars, as we have done in Fig. 6. This allows us to demonstrate again how closely the equilibrium line in the ρ-T diagram, the virial temperature, and the baryon fraction are connected.

The expected baryonic mass in a halo is given by

$$M_{\rm b} = \frac{4}{3}\,\pi\, r_{\rm vir}^3\, \overline{\rho}_{\rm b}, \tag{19}$$

where $\overline{\rho}_{\rm b}$ denotes the average gas density in a halo. At redshift $z = 0$, the majority of the gas is distributed at low densities along the power-law relation

$$\left(\frac{\rho_{\rm eq}}{\langle\rho\rangle_{\rm b}}\right)^{0.57} = \frac{T_{\rm eq}}{3.6\times10^3\ {\rm K}} \tag{20}$$

in the ρ-T phase diagram, where photo-heating balances adiabatic cooling due to the expansion of the universe. If we assume that the average temperature in halos is given by the virial temperature, then the average density (of the diffuse gas) in a halo cannot lie below the relation given by Eq. (20), i.e. this imposes a rough upper limit on the average gas density, and hence the diffuse baryonic content of the halo. With the help of Eq. (10), we can replace the virial temperature by the virial mass and cast this condition for the average gas density in a halo into

$$\left(\frac{\overline{\rho}_{\rm b}}{\langle\rho\rangle_{\rm b}}\right)^{0.57} = 9.7\times(z+1)\left\{\frac{\Delta_c(z)}{\Delta_c(0)}\right\}^{\frac{1}{3}}\left\{\frac{M_{\rm vir}}{10^{10}h^{-1}M_\odot}\right\}^{\frac{2}{3}}. \tag{21}$$

Plugging this result into Eq. (19) and using the definition of the virial radius, Eq. (1), we obtain

$$\frac{M_{\rm b}}{10^{10}h^{-1}M_\odot} = \frac{84.7}{\Delta_c(0)}\,\frac{\Omega_b}{\Omega_m}\left\{\frac{M_{\rm vir}}{10^{10}h^{-1}M_\odot}\right\}^{2.17}. \tag{22}$$

for the baryon mass at $z = 0$. The resulting baryon mass is shown in Fig. 6. Halos without any stellar matter are primarily distributed just above this line. Hence Eq. (22) provides a rough upper limit for the diffuse baryonic mass in dwarf-sized halos. In summary, for halos which contain virtually no condensed baryons, the diffuse gas mass can be determined from the equilibrium line in the ρ-T phase diagram. This can hence explain why halos significantly below $M_{\rm c}$ are seemingly almost empty of gas. It provides also a lower limit for the baryon fraction.

3.6 Condensation history

The basic argument above is that photo-ionisation can stop at some time the condensation process of gas in dwarf galaxy halos. We can support this idea further by finding halos with a constant amount of mass in the condensed phase. Figure 13 shows the evolution of the different mass components for two example halos. A halo selected with mass significantly above $M_{\rm c}$ at $z = 0$ has continuously increased the dark matter, stellar, and condensed masses, while the gas mass decreased. In a halo with total mass significantly below $M_{\rm c}$, the individual mass components change as well, but in contrast to the case of the more massive halo, the condensed mass is remarkably constant. This lends strong support to our basic argument. We see here that for the individual halo shown neither further gas condensates nor photo-heating evaporates all the gas. Thus even in the optically thin treatment of the galactic gas reservoir, photo-heating is not able to expel gas from the galaxy that has overdensities above ~ 1000. Instead, the condensed gas continues to be slowly converted into stars. It is thus not expected that photo-heating instantaneously switches off star formation.

We now analyse the mass accretion histories of several halos of different mass. In Fig. 14, we show that the evolution of the condensed phase changes systematically from halo masses below $M_{\rm c}$ to those above. For the latter, the total mass and the condensed mass grow almost in parallel. For halos with mass close to $M_{\rm c}$, the condensed mass increases

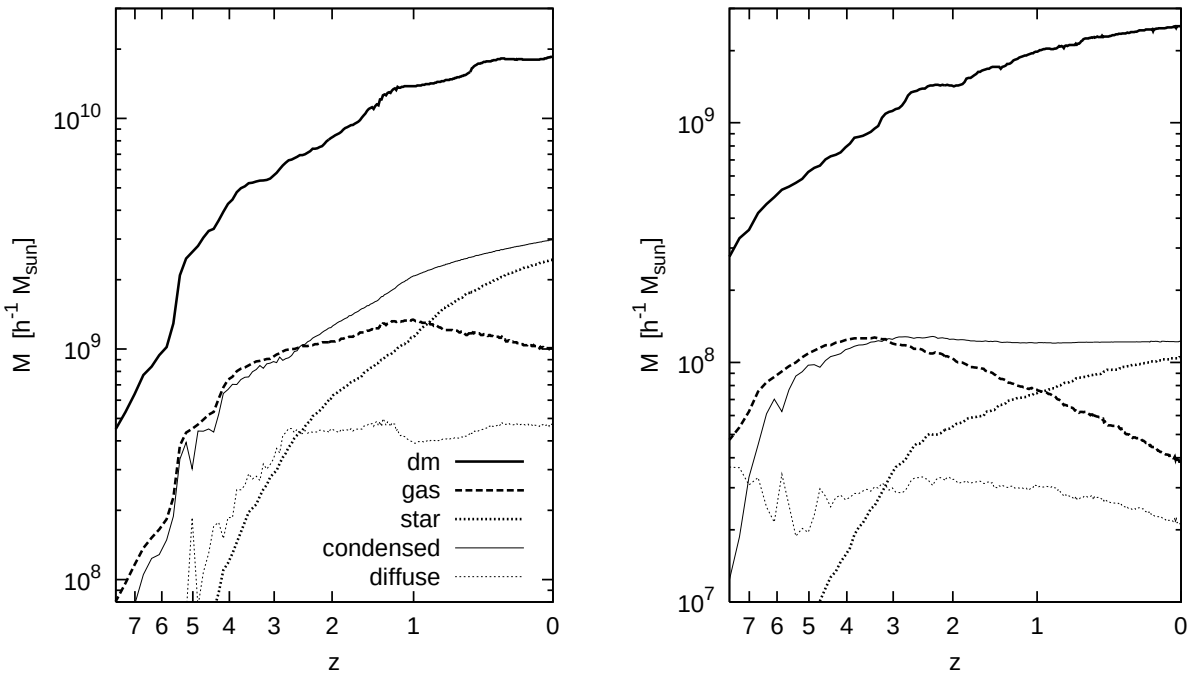

Figure 13. Evolution of the mass in different components for two high-resolution halos, one above $M_{\rm c}$ (left panel) and one below $M_{\rm c}$ (right panel). The evolution of the total mass (thick solid line), the condensed gas mass (thick dashed), the stellar mass (thick dotted) and diffuse gas mass (thin dotted) is shown. In addition the evolution of the condensed mass (gas+stars) is shown (thin solid line).

monotonically but slower than the total mass. Finally, for halos with mass significantly below $M_{\rm c}$, the condensed mass remains constant. Thus the evolution of individual halos is perfectly consistent with the result that photo-heating primarily stops condensation in small halos. Moreover, we find that our "refined" criterion for condensation reproduces the time at which condensation stops quite well. To show this explicitly we have plotted in the left panel of Fig. 14 $M_{\rm c}$ derived form $T_{\rm vir} = 1.3 \times T_{\rm entry}$. The times at which the low-mass halos fall below $M_{\rm c}$ correspond to the times at which the condensed masses begin to remain constant (right panel).

In halos with $M_{\rm tot}(0) \lesssim 2 \times 10^9 h^{-1} M_\odot$ the condensed gas phase is apparently evaporated completely. Even if these halo appear to be sufficiently well resolved at $z = 0$, we caution that condensation can only take place at $z \lesssim 4$, probably at even higher redshift since $M(z) < M_c(z)$. Hence we expect that in a simulation with higher resolution the condensed phase might stay and result in a noticeably larger amount of stars. However, we cannot really exclude that condensed gas in halos with $M_{\rm tot}(0) \lesssim 2 \times 10^9 h^{-1} M_\odot$ becomes generally unstable at some time and is therefore evaporated even for arbitrary good numerical resolution. Such an assumption is frequently invoked in simple analytic treatments. For instance, the analysis of Barkana & Loeb (1999) is based on the assumption that all gas with $T > T_{\rm vir}$ is evaporated. The fact that the significantly improved resolution of the 'high-res' run compared to the 'basic' run does not lead to a stable condensed gas phase in all halos with mass about $M_{\rm tot}(0) \sim 2 \times 10^9 h^{-1} M_\odot$ seems to point into this direction. However, more stringent test of this will require better resolution for the progenitor of these halos.

3.7 Stellar mass function

Using our estimates for the suppression of baryon condensation in halos with mass below $M_{\rm c}(z)$, an approximation for the expected stellar content in small halos may be derived. To this end we assume a mean mass accretion history for the small halos in our sample. Wechsler et al. (2002) and van den Bosch (2002) showed that the average dark matter mass accretion histories can be approximated by

$$M_{\rm MAH}(z) = M_{\rm tot}(z=0)\, e^{-\alpha z}, \qquad (23)$$

which works especially well for halos with an early formation time. In Fig. 14, we show an average accretion history (thin solid line) using $\alpha = 0.35$. Moreover, from the work of van den Bosch (2002) one can derive an appropriate value for α for halos with $\sim 5 \times 10^9\ h^{-1}\, M_\odot$ in a low density universe.

All halos in our sample have rather flat accretion histories compared to the evolution of the characteristic mass $M_{\rm c}(z)$, thus most of them have been able to condensate baryons and to form stars at high redshift. But at some time the halo mass fell below $M_{\rm c}(z)$, and from this time onwards the mass in the condensed phase is expected to remain constant. To test this, we estimate the stellar mass in a halo by computing first the redshift $z^{\rm eq}$ at which the mass according to the accretion history equals the characteristic mass, $M_{\rm MAH}(z^{\rm eq}) = M_{\rm c}(z^{\rm eq})$. At this redshift, we determine the condensed mass, assuming here that at this time the baryon fraction in the halos has the cosmic mean value Ω_b/Ω_m. In addition, we assume that on average 80 % of the baryons are in the condensed phase, see Fig. 13. Finally, as an upper limit for the amount of stars that may form, we assume that all of the condensed baryons are eventually converted into

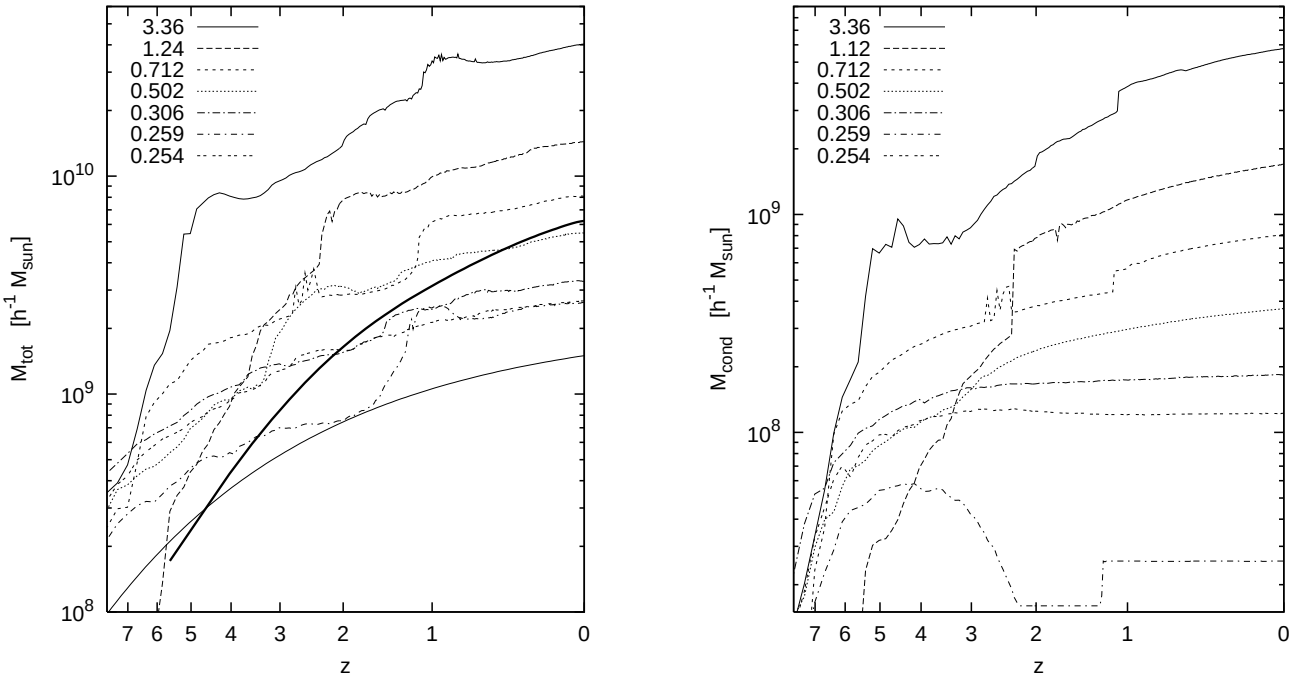

Figure 14. Mass accretion histories. We compute the mass accretion histories by choosing from the high-res run several halos at $z = 0$ and searching repeatedly for the most massive progenitor. The left panel shows the evolution of the total mass, while the right panel shows the evolution of the condensed baryon mass of the same halos. Jumps in the condensed mass indicate merger events. The numbers indicate the dark matter mass at $z = 0$ in $10^{10}\,h^{-1}\,M_\odot$. In the left panel, the evolution of the characteristic mass for the 'high-res' run is also shown (thick solid line). For comparison, we also plot the mean mass accretion history (thin solid line) for $M_{\rm tot} = 1.4 \times 10^9\,h^{-1}\,M_\odot$ with $\alpha = 0.35$, as expected for a low density environment, see Eq. (23).

stars, $\langle f_{\rm eq}\rangle = 0.8$. Hence we estimate the stellar mass in a given halo as $M_{\rm eq}(z=0) = \langle f_{\rm eq}\rangle\,\Omega_b/\Omega_m\,M_{\rm MAH}(z^{\rm eq})$. For halos more massive than $M_c(z=0)$ the maximum stellar mass is given just by $\langle f_{\rm eq}\rangle\,\Omega_b/\Omega_m\,M_{\rm tot}(0)$.

We define the stellar mass function, $N_{\rm halo}(M_*)$, as the number of halos with stellar mass larger than M_*, independent of the dark matter masses of the halos that host the galaxies. Figure 15 shows the stellar mass function obtained by the procedure described above (solid line). For comparison, we also show the mass function for a fixed stellar mass fraction f_* for all halos (dashed line). The deviation of the two curves below $M_* \sim 10^9\,h^{-1}\,{\rm M}_\odot$ indicates that in low-mass halos the stellar mass fraction falls below the fixed value f_*, hence those halos are shifted to smaller M_* and the mass function begins to flatten. For a stellar mass content of $\sim 10^8\,h^{-1}\,{\rm M}_\odot$ the number of halos is reduced by a factor of three. The simulated halo sample (dash-dotted line) provides a lower limit for the stellar mass function because of the limited numerical resolution. Above $\sim 10^8\,h^{-1}\,{\rm M}_\odot$, the two curves agree very well. For smaller masses, the two curves deviate since some halos have formed too few stars due to insufficient resolution. In conclusion, the photo-evaporation reduces the number of halos with $M_* \gtrsim 10^8\,h^{-1}\,{\rm M}_\odot$ by a factor of about four and, more importantly, the faint-end slope of the stellar mass function is much shallower than expected based on the dark halo mass function of N-body simulations alone.

4 DISCUSSION

The main purpose of this work has been to investigate the effect of UV-heating on the baryon fraction and the stellar mass of dwarf-sized isolated halos in voids. This is motivated by the suggestion that photo-heating may provide a potential explanation for the observed low number density of galaxies in voids, and the apparent paucity of luminous galactic satellites in the Local Group, in contrast to the large abundance of dark matter halos and subhalos, respectively, predicted by CDM models.

In order to examine this question, we have carried out some of the presently best resolved hydrodynamical simulations of galaxy formation in large regions of space. Our simulations are unique in the sense that they specifically sample cosmological void regions at high resolution and evolve them to the present epoch.

We have identified a characteristic mass scale below which the baryon fraction in a halo is reduced by photo-heating. This happens for masses $M_{\rm vir}(z=0) \lesssim 6.5 \times 10^9\,h^{-1}\,M_\odot$ (denoted here as dwarf galaxies), and this characteristic mass scale depends only weakly on the UV-flux. The suppression itself happens due to photo-evaporation of gas out of halos, thereby reducing the baryon fraction of dwarf galaxies, and also by offsetting cooling losses in halos such that further condensation of baryons is strongly reduced. We have derived a simple quantitative criterion that gives the characteristic mass $M_{\rm c}$ at which the baryon fraction is on average half that of the cosmic mean. This is phrased on a condition on the virial temperature which

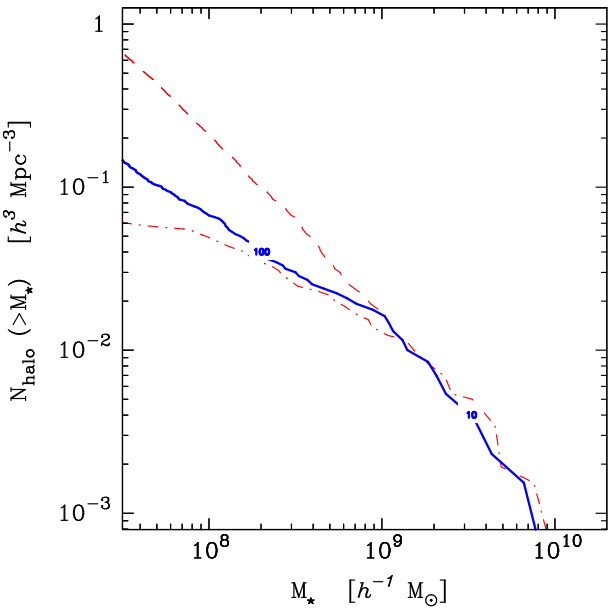

Figure 15. Stellar mass function at $z = 0$. We assign a stellar mass to each halo in the following manner: if $M_{\rm tot}(z = 0) > M_c(0)$ the stellar mass is $\langle f_* \rangle \Omega_b/\Omega_m \, M_{\rm tot}$. For smaller halos we compute the redshift z^* at which $M_{\rm tot} \exp(-\alpha z^*) = M_c(z^*)$. We compute the stellar mass according to $\langle f_* \rangle \Omega_b/\Omega_m \, M(z^*)$. The solid line show the results for the halo sample from the basic run and the parameters $\langle f_* \rangle = 0.8$ and $\alpha = 0.35$. Numbers along the line indicate how many halos are actually in our void sample. For comparison the stellar mass function obtained from the simulation (dash-dotted) is shown. In addition, we show the result for the assumption that in each halo the stellar mass amounts to $\langle f_* \rangle \Omega_b/\Omega_m \, M_{\rm tot}$ (dashed line).

must at least reach an "entry temperature" in the instable branch of the cooling/heating equilibrium line in the gas phase-space diagram. Our prediction for $M_c(z)$ is strikingly well in accord with the evolution obtained from the simulations.

At redshift $z = 0$, the characteristic mass scale of photo-evaporation corresponds to a circular velocity of $\sim 27\,{\rm km\,s^{-1}}$, which is significantly less than we would obtain with the filtering mass formalism introduced by Gnedin (2000) using an entirely different approach. We thus predict a considerably milder effect of photo-heating on the evolution of small halos. This has significant consequences for semi-analytic models of galaxy formation that relied on photo-heating as a feedback mechanism to suppress small galaxies. For instance, Somerville (2002) concluded that the substructure problem in the Local Group can be easily solved taking photo-evaporation into account, provided the effect is as strong as suggested by the analysis of Gnedin (2000). This conclusion is probably no longer valid when the effect is much weaker, as we find here.

It is clear however that the baryon fraction and hence the star fraction rate in void dwarf galaxies is significantly reduced by the UV-background. As a result, the halo mass function cannot be translated directly into a mass function of the luminous matter. In the framework of the physics included in our simulations, we argue that the baryonic mass belonging to a halo is essentially set at the time when $M_{\rm vir}(z) = M_c(z)$. We compute the resulting mass function of the stellar content in halos under this assumption and obtain good agreement with our direct simulation measurements.

We caution however that it is numerically difficult to resolve all the star formation in small dwarf galaxies at high redshift. While we have found some dwarf halos in our simulation without any stars, it seems plausible that this is due to insufficient resolution, because all halos with a progenitor with $M(z) > M_c(z)$ at some z should have been able to create some stars. Only in those halos with a very steep mass accretion history, steep enough to be for all redshifts below $M_c(z)$, star formation should always be suppressed.

Our results are derived under the assumption of optically thin gas with a spatially uniform UV flux, neglecting any effects due to self-shielding in the inner parts of halos. Recently, Susa & Umemura (2004a) analysed photo-evaporation with 3D radiation transfer simulations for individual halos. They found that for both a full radiation transfer treatment and a optical thin approximation the fast rising UV-background at high redshift efficiently suppresses star formation. However, a full radiation transfer treatment with self-shielding can only increase the amount of stars because it makes the UV heating less efficient. Neglecting self-shielding in our analysis may thus lead to an *overestimate* of the effects of the UV-background.

The evolution of the characteristic mass function depends essentially on the UV-flux history. We have used here the Haardt & Madau (1996) model, where reionisation takes place at redshift $z = 6$. Previous results from WMAP (Spergel et al. 2003) suggested that the Universe could have been reionised at much higher redshift. If true, the evolution of M_c could be much more shallow at high redshift. Consequently, more halos would have an accretion history entirely below $M_c(z)$, and hence more halos would remain virtually free of condensed baryons. The most recent analysis from three year data of WMAP (Spergel et al. 2006) indicates that reionisation took place in the redshift rage $z \sim 11$ to 7. This would lead to a moderately steeper $M_c(z)$. Interestingly, the so modified characteristic mass function would evolve almost parallel to the average accretion history, allowing both, halos which condensate gas only at high redshifts and others which start late to condensate. However, our measurements of the characteristic mass function based on the standard reionisation at $z = 6$ seem to be a good approximation for the effects of UV-heating in evaporating baryons of dwarf size halos.

In summary, it appears unlikely that adjustments in the reionisation history can alter our basic finding that UV-heating is not particularly efficient in evaporating all baryons out of dwarf-sized halos. This makes it questionable whether feedback by photo-heating is really sufficient to suppress dwarf galaxies in voids, luminous satellites in galaxies, and to flatten the faint end of the galaxy luminosity function as much as observationally indicated. Other proposed solutions like kinetic supernova feedback and associated galactic winds may therefore be needed to resolve these problems completely.

ACKNOWLEDGEMENTS

This work has been partially supported by the Acciones Integradas Hispano-Alemanas. MH and GY thanks financial support from the Spanish *Plan Nacional de Astronomia y Astrofisica* under project number AYA2003-07468. This research was supported in part by the National Science Foundation under Grant No. PHY99-0794. GY and SG thanks the Kavli Institut for Theoretical Physics for hospitality. We thank the John von Neumann Institute for Computing (Germany), the CIEMAT at Madrid (Spain), and the CLAMV at IU Bremen for kindly allowing us to use their computational facilities.

REFERENCES

Babul A., Rees M. J., 1992, MNRAS, 255, 346
Barkana R., Loeb A., 1999, ApJ, 523, 54
Bryan G. L., Norman M. L., 1998, ApJ, 495, 80
Carroll S. M., Press W. H., Turner E. L., 1992, ARA&A, 30, 499
Couchman H. M. P., Rees M. J., 1986, MNRAS, 221, 53
Dekel A., Rees M. J., 1987, Nature, 326, 455
Dekel A., Silk J., 1986, ApJ, 303, 39
Efstathiou G., 1992, MNRAS, 256, 43
Gnedin N. Y., 2000, ApJ, 542, 535
Gnedin N. Y., Hui L., 1998, MNRAS, 296, 44
Goldberg D. M., Jones T. D., Hoyle F., Rojas R. R., Vogeley M. S., Blanton M. R., 2005, ApJ, 621, 643
Gottlöber S., Łokas E. L., Klypin A., Hoffman Y., 2003, MNRAS, 344, 715
Grebel E. K., Gallagher J. S., 2004, ApJL, 610, L89
Gregory S. A., Thompson L. A., 1978, ApJ, 222, 784
Grogin N. A., Geller M. J., 1999, AJ, 118, 2561
Haardt F., Madau P., 1996, ApJ, 461, 20
Hoffman Y., Shaham J., 1982, ApJL, 262, L23
Joeveer M., Einasto J., Tago E., 1978, MNRAS, 185, 357
Katz N., Weinberg D. H., Hernquist L., 1996, ApJS, 105, 19
Kereš D., Katz N., Weinberg D. H., Davé R., 2005, MNRAS, 363, 2
Kirshner R. P., Oemler A., Schechter P. L., Shectman S. A., 1981, ApJL, 248, L57
Klypin A., Gottlöber S., Kravtsov A. V., Khokhlov A. M., 1999, ApJ, 516, 530
Klypin A., Kravtsov A. V., Bullock J. S., Primack J. R., 2001, ApJ, 554, 903
Klypin A., Kravtsov A. V., Valenzuela O., Prada F., 1999, ApJ, 522, 82
Kuhn B., Hopp U., Elsaesser H., 1997, A&A, 318, 405
Lindner U., Einasto M., Einasto J., Freudling W., Fricke K., Lipovetsky V., Pustilnik S., Izotov Y., Richter G., 1996, A&A, 314, 1
Mac Low M., Ferrara A., 1999, ApJ, 513, 142
Mateo M. L., 1998, ARA&A, 36, 435
Mathis H., White S. D. M., 2002, MNRAS, 337, 1193
Moore B., Ghigna S., Governato F., Lake G., Quinn T., Stadel J., Tozzi P., 1999, ApJL, 524, L19
Navarro J. F., Steinmetz M., 1997, ApJ, 478, 13
Navarro J. F., Steinmetz M., 2000, ApJ, 538, 477
Peebles P. J. E., 1982, ApJL, 263, L1
Peebles P. J. E., 2001, ApJ, 557, 495
Popescu C. C., Hopp U., Elsaesser H., 1997, A&A, 325, 881
Power C., Navarro J. F., Jenkins A., Frenk C. S., White S. D. M., Springel V., Stadel J., Quinn T., 2003, MNRAS, 338, 14
Rees M. J., 1986, MNRAS, 218, 25P
Somerville R. S., 2002, ApJ, 572, L23
Spergel D. N., Bean R., Dore' O., et al. 2006, ArXiv Astrophysics e-prints
Spergel D. N., Verde L., Peiris H. V., Komatsu E., Nolta M. R., Bennett C. L., Halpern M., Hinshaw G., Jarosik N., Kogut A., Limon M., Meyer S. S., Page L., Tucker G. S., Weiland J. L., Wollack E., Wright E. L., 2003, ApJS, 148, 175
Springel V., Hernquist L., 2002, MNRAS, 333, 649
Springel V., Hernquist L., 2003, MNRAS, 339, 289
Springel V., Yoshida N., White S. D. M., 2001, New Astronomy, 6, 79
Susa H., Umemura M., 2004a, ApJ, 600, 1
Susa H., Umemura M., 2004b, ApJL, 610, L5
Tassis K., Abel T., Bryan G. L., Norman M. L., 2003, ApJ, 587, 13
Thoul A. A., Weinberg D. H., 1996, ApJ, 465, 608
Umemura M., Ikeuchi S., 1984, Prog. Theor. Phys., 72, 47
van de Weygaert R., van Kampen E., 1993, MNRAS, 263, 481
van den Bosch F. C., 2002, MNRAS, 331, 98
Wechsler R. H., Bullock J. S., Primack J. R., Kravtsov A. V., Dekel A., 2002, ApJ, 568, 52
Yepes G., Kates R., Khokhlov A., Klypin A., 1997, MNRAS, 284, 235